MA-LIO: Multiple Asynchronous LiDAR-Inertial Odometry with Time-dependent Point-wise Uncertainty

Minwoo Jung
Department of Mechanical Engineering
Seoul National University
Seoul, S. Korea
Email: moonshot@snu.ac.kr

Sangwoo Jung
Department of Mechanical Engineering
Seoul National University
Seoul, S. Korea
Email: dan0130@snu.ac.kr

Ayoung Kim
Department of Mechanical Engineering
Seoul National University
Seoul, S. Korea
Email: ayoungk@snu.ac.kr

***Abstract*—Recently, multiple Light Detection and Ranging (LiDAR) systems have seen increased usage due to their amplified accuracy and stability from an expanded field of view (FOV). Nevertheless, combining multiple LiDARs presents a challenge due to temporal and spatial differences. Common practice is transforming points among sensors while requiring strict time synchronization or approximating transformation among sensor frames. Unlike existing methods, we exploit continuous-time (CT) inertial measurement unit (IMU) modeling to elaborate inter-sensor transformation and derive associated ambiguity as a point-wise uncertainty achieved by combining state covariance with the acquisition time and point range. It lessens the need for strict time synchronization and overcomes FOV differences. We validated our method on several datasets, and it is compatible with various LiDAR manufacturers and scanning patterns.**

I. Introduction & Related Works

Over the last decades, robot navigation using LiDAR has substantially advanced localization and map construction. Although existing methods mostly solve for a single LiDAR system, limited FOV and occlusion lead to a need for multiple LiDARs. When integrating multiple LiDARs in a complementary configuration, two significant challenges impede naive integration, namely temporal and spatial discrepancy.

***(i)* Synchronization:** A tempting and straightforward approach to integrating measurements is to enforce strict time synchronization among sensors, as exemplified by M-LOAM [8]. This can be performed by Pulse per Second (PPS) via external hardware and Precision Time Protocol (PTP); however, their support varies among manufacturers, necessitating compatible sensor combinations. Due to this sophisticated setting for synchronization, some asynchronous public datasets [4, 5, 15, 16] require software solutions to handle temporal discrepancies; however, some of the solutions [16, 10] induced information loss and error in degenerate environments. Nguyen et al. [14] and Wang et al. [17] exploited the IMU to compensate for temporal discrepancies. The idea of utilizing IMU was affordable; still, the error originating from discrete propagation remains. Some researchers suggested using optimization in continuous-time formulation [11, 13]. While this approach can estimate the entire trajectory at anytime, its computational intensity limits real-time viability. Our method sets itself apart by utilizing all available data, including asynchronous scans, while avoiding linear approximation. B-Spline interpolation is used instead to estimate each LiDAR measurement trajectory, offering a computationally efficient solution for multi-LiDAR SLAM in real-world environments.

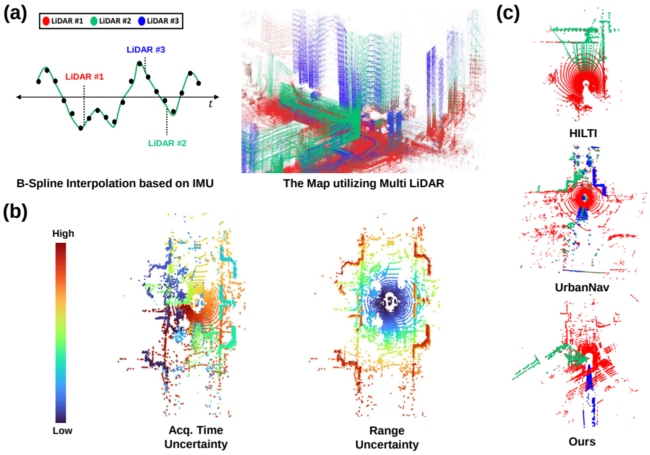

Fig. 1: (a) CT IMU interpolation enables us to merge points accurately, thus substantially increasing net FOV in the accumulated map. (b) Two types of uncertainties are considered in this paper (c) Example of FOV difference in multi-LiDAR datasets.

***(ii)* Spatial discrepancy:** Another solution for the temporal discrepancy is to apply scan matching for correction. However, different scanning patterns and small FOVs can create spatial discrepancies, challenging this approach. Specifically, non-repetitive scanning patterns [4] and obliquely installed LiDARs [5] can lead to little overlapping area among sensors.

***(iii)* Uncertainty propagation:** The projection of points among sensors incurs ambiguity due to the two discrepancies. Proper uncertainty modeling can mitigate it across multiple LiDARs. Recent research on LiDAR uncertainty focuses on learning-based methods [2, 12, 9, 7]. Yet, like ours, model-based strategies [17, 8, 1, 6] are also present. We assign point-wise uncertainty based on range and acquisition time, differing from the existing approach [17], which weights LiDAR residuals using IMU and LiDAR odometry discrepancies. Similar to M-LOAM [8], our method utilizes state covariance and point-wise uncertainty [1]. However, it is more flexible, not requiring inter-LiDAR overlap for covariance update.

This paper introduces an asynchronous multiple LiDAR-inertial odometry approach (Fig. 2), designed to overcome aforementioned multi-LiDAR challenges. We model point-wise uncertainty using the range and state covariance at each time and calculate the localization weight based on the surrounding environment for optimization. We efficiently

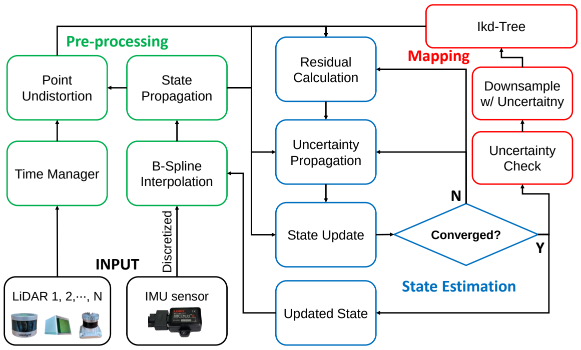

Fig. 2: Our proposed method is threefold: pre-processing, state estimation, and mapping. Pre-processing combines and undistort points via B-spline interpolation. The state estimation manages point-wise uncertainty and applies IESKF until convergence. The optimal state is then used in the IMU model for subsequent precise interpolation. Finally, points are projected into an ikd-Tree based on uncertainty.

handle a large volume of points by employing the ikd-Tree [19] and an Iterative Error State Kalman Filter (IESKF). Our contributions are as follows:

1) We tackle FOV discrepancy by accurately transferring points among LiDARs and using CT interpolation to lessen temporal discrepancies, ensuring consistent inter-LiDAR scan alignment despite large FOV variations.
2) Our method captures increased uncertainty at point-level based on range and acquisition time, providing a broader uncertainty management approach.
3) The localization weight balances prior and measurement residuals during optimization, adjusting automatically in degenerate environments such as narrow corridors.

II. METHOD

A. The Notion and State

Subscript A in notation $()_A$ denotes the representing frame. The frame B in frame A is denoted as $()_{AB}$. The ground truth is represented as $()$, while propagated, error, and optimal state are denoted as $\widehat{()}$, $\widetilde{()}$, and $\bar{()}$. For simplicity, we classify N LiDARs as $\{L_i, i=1,\cdots,N\}$, designating the LiDAR with the latest sample point as P and all other LiDARs as S. Our system comprises a state $\mathbf{x}$, input $\mathbf{u}$, and noise $\mathbf{w}$ as

$$\begin{aligned}\mathcal{M} &\triangleq SO(3)\times\mathbb{R}^{15}\times\Pi_{i=1}^{N}\left(SO(3)\times\mathbb{R}^{3}\right)\\ \mathbf{x} &\triangleq \begin{bmatrix}\mathbf{R}_{GI}^{T} & \mathbf{t}_{GI}^{T} & \mathbf{v}_{GI}^{T} & \mathbf{b}_{\omega}^{T} & \mathbf{b}_{a}^{T} & \mathbf{g}_{G}^{T} & \mathbf{R}_{IL_i}^{T} & \mathbf{t}_{IL_i}^{T}\end{bmatrix}^{T}\in\mathcal{M}\\ \mathbf{u} &\triangleq \begin{bmatrix}\omega_m^T & a_m^T\end{bmatrix}^T, \mathbf{w}\triangleq\begin{bmatrix}n_\omega^T & n_a^T & n_{b\omega}^T & n_{ba}^T\end{bmatrix}^T. \qquad (1)\end{aligned}$$

For the state $\mathbf{x}$, transformation of the IMU frame (denoted as I) in the global frame (denoted as G) is $\mathbf{T}_{GI}=(\mathbf{R}_{GI},\mathbf{t}_{GI})$, which consists of the rotation and translation. Additionally, $\mathbf{v}$, $\mathbf{g}$, and $\mathbf{b}$ stand for velocity, gravity, and bias, while $\mathbf{T}_{IL}$ denote the extrinsic between LiDAR and IMU.

B. IMU Discrete Model with B-Spline Interpolation

The CT kinematic model can be converted into a discrete model using the $\boxplus$ outlined in [19] with the function $\mathbf{f}$. Here, function $\mathbf{f}$ transitions the system state with a parameterized discretization interval Δt. During the time interval between $(i-1)$ and $(i)^{\text{th}}$ scans, the system estimates the trajectory using the IMU, assuming the $(i-1)^{\text{th}}$ state to be optimal.

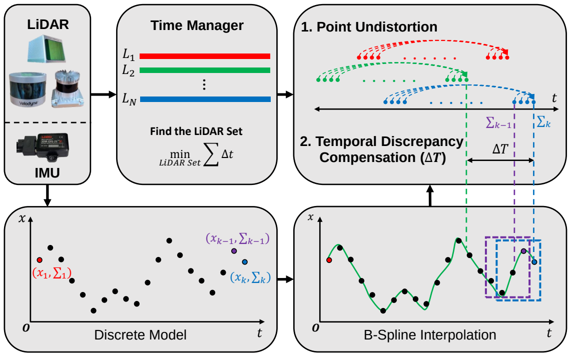

Fig. 3: IMU inputs are propagated and fed into B-spline interpolation. The LiDAR with minimal time differences is selected. This facilitates *(i)* undistortion of a LiDAR pointcloud into a single frame and *(ii)* compensation for temporal discrepancy using relative transformations among the last points in each LiDAR.

$$\begin{aligned}\widehat{\mathbf{x}}_{k+1} &= \widehat{\mathbf{x}}_k\boxplus\left(\Delta t\mathbf{f}\left(\widehat{\mathbf{x}}_k,\mathbf{u}_k,\mathbf{0}\right)\right);\ \widehat{\mathbf{x}}_0=\bar{\mathbf{x}}_{i-1} \qquad (2)\\ \widehat{\Sigma}_{k+1} &= \mathbf{F}_{\tilde{\mathbf{x}}_k}\widehat{\Sigma}_k\mathbf{F}_{\tilde{\mathbf{x}}_i}^T+\mathbf{F}_{\mathbf{w}_k}\mathbf{Q}_k\mathbf{F}_{\mathbf{w}_i}^T;\ \widehat{\Sigma}_0=\bar{\Sigma}_{i-1} \qquad (3)\end{aligned}$$

, where $\mathbf{Q}_k$ denotes the covariance of $\mathbf{w}_k$ while the jacobians $\mathbf{F}_{\tilde{\mathbf{x}}_k}$ and $\mathbf{F}_{\mathbf{w}_k}$ represent the derivatives of $(\mathbf{x}_{k+1}\boxminus\widehat{\mathbf{x}}_{k+1})$ with respect to each subscript, under the conditions that $(\tilde{\mathbf{x}}_k, w_k)=(0,0)$. Also, $\widehat{\mathbf{x}}_{k-1}$ can be achieved using the $\boxminus$ operator as detailed in [18]. Since the IMU discrete model before optimization may not be accurate, the IMU state preceding $\bar{\mathbf{x}}_{i-1}$ is recalculated via $\boxminus$ operator for the accurate interpolation.

Based on propagation, B-spline interpolation is performed using four transformations, known as control points from $\mathbf{T}_{GI}^{k-1}$ to $\mathbf{T}_{GI}^{k+2}$ [13]. By this interpolation, trajectory at any time can be estimated, which is especially beneficial for asynchronous sensors. The transformation at time $t\in[t_k,t_{k+1})$ is

$${}^{B}\mathbf{T}_{GI}\left(s\left(t\right)\right)=\mathbf{T}_{GI}^{k-1}\Pi_{n=1}^{3}\exp\left(\tilde{\mathbf{B}}_j\left(s\left(t\right)\right)\Omega_{k+n-1}\right) \qquad (4)$$

, while variables can be seen in [13]. The notation ${}^{B}\mathbf{T}$ means that it is calculated by B-spline. Lastly, $\widehat{\Sigma}_{k+1}$ is assigned to ${}^{B}\mathbf{T}$ computed at $t\in[t_k,t_{k+1})$ as its covariance (Fig. 3).

C. LiDAR Preprocessing with Uncertainty Propagation

Despite the strict interpolation, the interpolated pose accuracy is directly affected by the minimum difference in arrival times among LiDARs. Therefore, a set of LiDAR is chosen to minimize the sum of differences in the arrival times.

For undistortion, we focus on LiDAR S, which is samely applied to LIDAR P. Relative transformations between frames merge points from different times into one frame. By using B-spline interpolation, point p_{S^j} at time t_j gets transformed to LiDAR frame at t_l, yielding undistorted point $p_{S^j}^u$.

$$p_{S^j}^u=\mathbf{T}_{IS}^{-1}{}^{B}\mathbf{T}_{I^lI^j}\mathbf{T}_{IS}p_{S^j}, \qquad (5)$$

, where t_l is the latest arrival time in S, and u identifies the undistorted point. Then, the temporal discrepancies due to different arrival times are compensated for each LiDAR. The latest arrival time (t_i) of the latest LiDAR P (blue point in Fig. 3) is leveraged to transform points from other LiDARs.

$$p_{P^iS^j}=\mathbf{T}_{IP}^{-1}{}^{B}\mathbf{T}_{I^iI^l}\mathbf{T}_{IS}p_{S^j}^u=\mathbf{T}_{IP}^{-1}{}^{B}\mathbf{T}_{I^iI^j}\mathbf{T}_{IS}p_{S^j}. \qquad (6)$$

This transformation incorporates both undistortion and temporal compensation over multiple frame changes, and errors associated with these changes may accumulate.

The uncertainty must be propagated to each point using the covariance to include the errors in the optimization. Covariances of ${}^{B}\mathbf{T}$ and $\mathbf{T}_{IL}$ are achieved by (3) and IESKF. Also, the covariance of inverse transformation is calculated through $\Sigma_{inv} = T \Sigma T^{T}$, where T is the adjoint matrix of $\mathbf{T}^{-1}$. With fourth-order approximation, the transformation and covariance can be combined into $\{\mathbf{T}_{P^i S^j}, \Sigma_{P^i S^j}\}$ [1], which tr$(\Sigma_{P^i S^j})$ is the acquisition time uncertainty visualized in Fig. 1.

Our improvements over previous research are twofold. We assign uncertainty based on acquisition time, unlike [8], enabling more precise uncertainty modeling. Also, we eliminate the need to designate a primary LiDAR. By employing extrinsic covariances between LiDAR and IMU, we sidestep the issue of secondary LiDAR exhibiting higher covariance than the primary one, thus ensuring an equal impact on all LiDARs. The transformed point into the frame P is presented as

$$\begin{aligned} p_{P^i S^j} &\triangleq \widehat{\mathbf{T}}_{P^i S^j} \widehat{p}_{S^j} = \exp\left(\xi^{\wedge}_{P^i S^j}\right) \mathbf{T}_{P^i S^j} \left(p_{S^j} + D\zeta\right) \\ &\approx \left(I + \exp\left(\xi^{\wedge}_{P^i S^j}\right)\right) \mathbf{T}_{P^i S^j} \left(p_{S^j} + D\zeta\right) \end{aligned} \tag{7}$$

Here, ξ is the transformation error, and $\zeta \in \mathbb{R}^3$ is the measurement perturbation. Also, p in (7) is a 4×1 vector with a scale value 1 added, and D is the dilation matrix which transforms the dimension from 3×1 to 4×1, with zero terms added. We only consider the first-order term, $\widehat{\mathbf{T}}\widehat{p} \approx \mathbf{q} + \mathbf{Q}\theta$

$$\begin{aligned} \mathbf{q} &:= \mathbf{T}p,\ \mathbf{Q} := \left[(\mathbf{T}p)^{\odot}\ \ \mathbf{T}D\right],\ \begin{bmatrix} \epsilon \\ \eta \end{bmatrix}^{\odot} := \begin{bmatrix} \eta\mathbf{1} & -\epsilon^{\wedge} \\ \mathbf{0}^T & \mathbf{0}^T \end{bmatrix} \quad (8) \\ \theta &:= \begin{bmatrix} \xi^T & \zeta^T \end{bmatrix}^T,\ \theta \sim \mathcal{N}\left(\mathbf{0}, \Xi\right),\ \Xi = \text{diag}\left(\Sigma_{P^l S^j}, \mathbf{Z}\right) \end{aligned}$$

with the LiDAR measurement covariance $\mathbf{Z}$. As $p_{P^i S^j}$ follows the Gaussian distribution, the uncertainty of the point can be obtained as $\Sigma_p = \mathbf{Q}\Xi\mathbf{Q}^T$. The uncertainty is derived from the point range from $(\mathbf{T}p)^{\odot}$, and the acquisition time from $\Sigma_{P^l S^j}$.

D. Iterated Error State Kalman Filter

Our system utilizes a plane measurement model, assuming local planarity. The plane consists of the five closest neighboring points from the measurement in the ikd-Tree, accounting for point uncertainty in the measurement model. The notation L is used to denote the LiDAR, S or P. The weighted covariance of the plane for point p_{L^j}, Σ_{L^j}, is computed as

$$\Sigma_{L^j} = \sum_{n=1}^{5} w_n^2 \Sigma_n, \quad w_n = \frac{\tau - \text{tr}\left(\Sigma_n\right)}{\sum_{n=1}^{5}\left[\tau - \text{tr}\left(\Sigma_n\right)\right]} \tag{9}$$

, while τ represents the uncertainty threshold. Based on the normal vector of the plane, $\mathbf{v}_{GL^j}$, and the plane covariance, Σ_p, the measurement model is calculated as

$$\mathbf{h}_{L^j}\left(\mathbf{x}_i,\, \mathbf{n}_{L^j}\right) = \frac{\mathbf{v}_{GL^j}^T \left(\mathbf{T}_{GI^i}\, {}^{B}\mathbf{T}_{I^i I^l} \mathbf{T}_{IL}\left(\mathbf{p}_{L^j}^u + \mathbf{n}_{L^j}\right) - \mathbf{q}_{GL^j}\right)}{\text{FIC}\left(\text{tr}\left(\Sigma_{L^j}\right), s_{max}, s_{min}\right)}. \tag{10}$$

Here, $\mathbf{n}_{L^j}$ represents the noise from the LiDAR, and $\mathbf{q}_{GL^j}$ is a point located on the plane. Additionally, $\mathbf{h}$ represents the measurement model, which is a summary of the terms of state, including $\mathbf{T}_{GI}$ and $\mathbf{T}_{IL}$. We employ fixed interval conversion (FIC) to bind the uncertainty, which is calculated as

$$\text{FIC}(V, I_{max}, I_{min}) = \frac{(I_{max} - I_{min})(V - V_{min})}{V_{max} - V_{min}} + I_{min}, \tag{11}$$

with I_{max} and I_{min} to be the rescaling interval. Utilizing FIC, we balance V within set boundaries V_{max} and V_{min}, enhancing reliability without overemphasis or neglect.

The state propagation component, as represented in equations (2) and (3), is utilized as the prior distribution, and its error state is obtained through

$$\mathbf{x}_i \boxminus \widehat{\mathbf{x}}_i = \left(\widehat{\mathbf{x}}_i^{\kappa} \boxplus \tilde{\mathbf{x}}_i^{\kappa}\right) \boxminus \widehat{\mathbf{x}}_i = \widehat{\mathbf{x}}_i^{\kappa} \boxminus \widehat{\mathbf{x}}_i + \mathbf{J}^{\kappa}\tilde{\mathbf{x}}_i^{\kappa} \sim \mathcal{N}(\mathbf{0}, \widehat{\Sigma}_i). \tag{12}$$

$\mathbf{J}^{\kappa}$ represents the Jacobian matrix of $\left(\widehat{\mathbf{x}}_i^{\kappa} \boxplus \tilde{\mathbf{x}}_i^{\kappa}\right) \boxminus \widehat{\mathbf{x}}_i$ with the condition that $\tilde{\mathbf{x}}_i^{\kappa} = 0$. When $\kappa = 1$, $\mathbf{J}^{\kappa} = \mathbf{I}$ and transformation term in $\widehat{\mathbf{x}}_i$ becomes ${}^{B}\mathbf{T}_{GI^i}$. Further details are as in [18].

In the case of the measurement model, another distribution can be identified through a first-order approximation:

$$\begin{aligned} \mathbf{0} &= \mathbf{h}_{L^j}\left(\mathbf{x}_i, \mathbf{n}_{L^j}\right) \simeq \mathbf{h}_{L^j}\left(\widehat{\mathbf{x}}_i^{\kappa}, \mathbf{0}\right) + \mathbf{H}_{L^j}^{\kappa}\tilde{\mathbf{x}}_k^{\kappa} + \mathbf{v}_{L^j} \\ -\mathbf{v}_j &= \mathbf{z}_{L^j}^{\kappa} + \mathbf{H}_{L^j}^{\kappa}\tilde{\mathbf{x}}_k^{\kappa} \sim \mathcal{N}\left(\mathbf{0}, \Sigma_{L^j}\right) \end{aligned} \tag{13}$$

, where $\mathbf{H}_{L^j}^{\kappa}$ is the Jacobian of $\mathbf{h}_{L^j}\left(\widehat{\mathbf{x}}_i^{\kappa} \boxplus \tilde{\mathbf{x}}_i^{\kappa}, \mathbf{n}_{L^j}\right)$ with $\tilde{\mathbf{x}}_i^{\kappa}$, and $\mathbf{v}_j$ is the noise with covariance calculated as in (8). Using prior (12) and measurement distribution (13), the estimation problem is changed into maximum a posteriori (MAP):

$$\min_{\tilde{\mathbf{x}}_i^{\kappa}} \left(\|\mathbf{x}_i \boxminus \widehat{\mathbf{x}}_i\|^2_{\widehat{\Sigma}_i} + w_l^2 \sum_{L=P,S} \sum_{j=1}^{m} \|\mathbf{z}_{L^j}^{\kappa} + \mathbf{H}_{L^j}^{\kappa}\tilde{\mathbf{x}}_i^{\kappa}\|^2_{\mathbf{R}_{L^j}} \right) \tag{14}$$

, while $\mathbf{R}_{L^j}$ is the output from FIC$(\text{tr}(\Sigma_{L^j}), \mathbf{R}_{max}, \mathbf{R}_{min})$, and $\|\mathbf{x}\|^2_{\Sigma} = \mathbf{x}^T\Sigma^{-1}\mathbf{x}$. The localization weight, w_l, balances prior distribution over measurements, particularly in degenerated environments. w_l can be computed from the ratio of σ_1 to σ_3 from Singular Value Decomposition (SVD) of measurement normal vector. If w_l exceeds the boundaries of (b_{min}, b_{max}), w_l is set as l_{min} or l_{max} respectively; otherwise, it is same as FIC(w, l_{max}, l_{min}). An iterated Kalman filter can solve the MAP problem with convergence criteria $\|\widehat{\mathbf{x}}_i^{\kappa+1} \boxminus \widehat{\mathbf{x}}_i^{\kappa}\| < \epsilon$, and its estimates for state and covariance are detailed in [18].

After optimization, if the uncertainty of a point, tr(Σ_{L^j}), surpasses τ, it is not saved in the tree. Unlike the ikd-Tree, our strategy accounts for uncertainty during insertion. If the insertion point is within the diagonal of Z at the center of the tree, we retain lower uncertainty points in our implementation.

III. EXPERIMENT

A. Dataset and Evaluation

To evaluate the performance of our method, we experimented with three datasets: Hilti SLAM Dataset 2021 [4], UrbanNav [5], and our dataset, collected using OS2-128, Livox Avia and Tele. It involves challenging environments at higher speeds (about 50 km/h) with U-turns and tunnels.

Our method is compared with state-of-the-art methods including Fast-LIO2 (single) [19], M-LOAM (multi) [8], and LOCUS 2.0 (multi) [16]. Fast-LIO2 utilizes the central LiDAR ,which provides the most points. For the Hilti dataset, we collect the trajectory from each LiDAR, OS0-64 (Fast-O),

TABLE I: APE for Hilti SLAM Dataset 2021

	Ours	Fast-H	Fast-O	M-LOAM	LOCUS 2.0
Basement	**0.036**	0.709	*0.046*	0.115	0.120
Campus	**0.046**	0.063	*0.063*	0.386	0.087
Construct	**0.063**	0.200	*0.088*	2.647	0.290
LAB	**0.024**	Err	*0.026*	0.064	0.040
UZH	**0.177**	0.233	0.184	0.276	*0.177*

The best results are in **bold** and the second-best's are in *italic*.

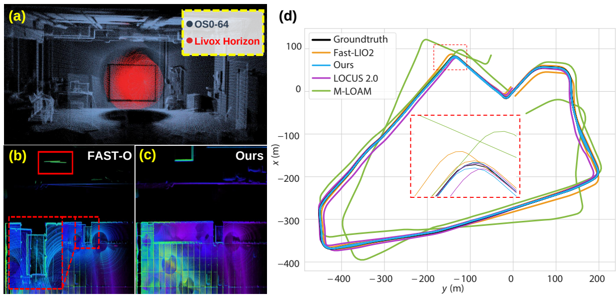

Fig. 4: (a) Accumulated scans from LAB. Compared to Ouster (gray), Livox (red) reveals limited FOV and causes localization failure. (b-c) show the outputs of Fast-O and our method for the Parking dataset. As shown in the red box in (b), the map produced by Fast-O is misaligned when returning to the starting point, while our result in (c) is well aligned. (d) represents the trajectory produced from all methods in Mongok.

and Livox Horizon (Fast-H). Performance is quantitatively compared by calculating the Root Mean Square Error (RMSE) of the Absolute Pose Error (APE) [m] and Relative Pose Error (RPE) [%] using the Evo evaluator [3]. For the Hilti dataset, we use its evaluator for the APE. For our dataset, the ground truth is sourced from an Inertial Navigation System (INS).

B. Quantitative Evaluation

In the Hilti dataset, our method consistently yields the highest accuracy across all sequences according to the results in Table. I. Fast-O ranks second in most cases, impressively without multi-LiDAR usage. M-LOAM and LOCUS 2.0 are less accurate than the others due to the absence of inter-LiDAR synchronization. This lack of synchrony is less impactful in LAB and UZH, with fewer movements, but causes higher errors in Campus and Construct. Still, our method maintains robustness thanks to temporal compensation. Fast-H degrades a phenomenon attributed to the limited FOV of LiDAR, leading to tracking deviation. In this perspective, Fast-O seems the best choice; however, it induces error in the Parking sequence due to the short detection range. Our method overcomes this by utilizing additional LiDAR, showing the strength of a multi-LiDAR system, as evidenced in Fig. 4(b) and (c).

The results on UrbanNav and our dataset are presented in Table. II. Our method demonstrates the most impressive results. The trajectory becomes more inaccurate for M-LOAM and LOCUS 2.0 due to errors arising from the asynchrony under high-speed movement vehicle. For the UrbanNav dataset, two inclined LiDARs allow a wider FOV. It allows for a number of measurements that cannot be observed with the central LiDAR, resulting in high accuracy as shown in Fig. 4(d).

Additionally, City01-03 includes challenging environments such as a 4.3km route, a tunnel, and numerous dynamic objects. While this makes the error higher than other datasets, our method still achieves the highest accuracy. In City02, our method successfully estimated the state even in a 400m tunnel. Despite the various difficulties, ours maintained the performance, demonstrating its reliability and robustness.

TABLE II: UrbanNav and Our Dataset Evaluation

		Fast-LIO2	M-LOAM	LOCUS 2.0	Ours
Mongok	APE	*5.917*	25.899	6.846	**2.579**
	RPE	0.188	0.632	*0.174*	**0.167**
Whampoa	APE	*7.066*	31.482	18.124	**4.236**
	RPE	0.390	0.710	*0.339*	**0.207**
TST	APE	*8.783*	53.682	33.292	**2.342**
	RPE	*0.494*	2.177	0.841	**0.351**
City01	APE	*9.970*	33.907	23.998	**6.538**
	RPE	*0.292*	0.955	0.609	**0.266**
City02	APE	*35.308*	72.382	58.211	***6.707***
	RPE	*0.608*	3.665	1.531	**0.565**
City03	APE	*6.951*	33.801	21.753	**5.470**
	RPE	*0.996*	1.310	1.159	**0.565**

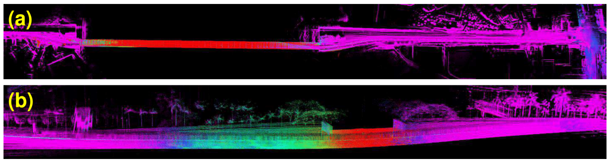

Fig. 5: Partial maps of (a) City02 and (b) Whampoa display points color-coded by localization weight, ranging from low (red) to high (pink). Both maps exhibit an apparent weight decrease in tunnel regions, with (b) showing a less significant decrease due to the upper part of the underpass being open and scanned by inclined LiDAR.

C. Ablation Study

***(i)* Localization weight:** In Fig. 5, we depict partial maps of the City02 and Whampoa. The narrow nature of these environments may result in correspondence error, leading to prior residuals having a stronger influence than measurement residuals. As seen in Fig. 5(a) and (b), localization weight is noticeably reduced only in degenerate surroundings, which is expected and highlights the effectiveness of our localization weight in such challenging environments.

***(ii)* The number of LiDAR:** We analyze the impact of the number of LiDAR on computation time and accuracy. In Whampoa and City03, featuring the most extensive distance among each dataset, our method consumes 47.7 and 79 ms to support 10Hz, with three LiDARs. For accuracy, we evaluate our method in two datasets. In Whampoa and City03, APE decreases as the number of LiDAR increase, with (5.69, 4.01, **3.58**) and (5.65, 5.08, **4.73**). Notably, a significant error reduction is observed when increasing the number of LiDAR from one to two, while a minor reduction is seen when increasing from two to three. This is because an increment to two LiDARs provides sufficient constraint. Furthermore, it may be a fallacy to posit that more LiDARs necessarily give better performance. In City03, adding the Livox Avia and Tele does not effectively reduce error due to their narrow FOV and wide overlap with Ouster LiDAR. It emphasizes the importance of LiDAR placement in a multi-LiDAR system.

IV. CONCLUSION

We proposed a framework for asynchronous multiple LiDAR-inertial systems. Based on B-spline interpolation, it handles temporal discrepancy among multiple LiDARs, and models point-wise uncertainty to avoid ambiguity accumulation. Furthermore, localization weight is utilized for enhanced performance in challenging conditions. Our method, validated on public and our datasets, offers real-time performance and outperforms the state-of-the-art in accuracy and robustness..

Acknowledgments

This research was conducted with the support of the ”National R&D Project for Smart Construction Technology (23SMIP-A158708-04)” funded by the Korea Agency for Infrastructure Technology Advancement under the Ministry of Land, Infrastructure and Transport, and managed by the Korea Expressway Corporation.

References

[1] T. Barfoot and P. Furgale. Associating uncertainty with three-dimensional poses for use in estimation problems. *IEEE Transactions on Robotics*, 30(3):679–693, 2014. URL https://ieeexplore.ieee.org/abstract/document/6727494.

[2] Di Feng, Lars Rosenbaum, and Klaus Dietmayer. Towards safe autonomous driving: Capture uncertainty in the deep neural network for lidar 3d vehicle detection. In *Proceedings of the IEEE Intelligent Transportation Systems Conference*, pages 3266–3273, 2018. URL https://ieeexplore.ieee.org/abstract/document/8569814.

[3] M. Grupp. Evo: Python package for the evaluation of odometry and slam., 2017. URL https://github.com/MichaelGrupp/evo.

[4] M. Helmberger, K. Morin, B. Berner, N. Kumar, G. Cioffi, and D. Scaramuzza. The hilti slam challenge dataset. *IEEE Robotics and Automation Letters*, 7(3):7518–7525, 2022. URL https://ieeexplore.ieee.org/abstract/document/9797800.

[5] L. Hsu, N. Kubo, W. Wen, W. Chen, Z. Liu, T. Suzuki, and J. Meguro. Urbannav: An open-sourced multisensory dataset for benchmarking positioning algorithms designed for urban areas. In *ION GNSS+*, pages 226–256, 2021. URL https://www.ion.org/publications/abstract.cfm?articleID=17895.

[6] B Jiang and S Shen. A lidar-inertial odometry with principled uncertainty modeling. In *Proceedings of the IEEE/RSJ International Conference on Intelligent Robots and Systems*, pages 13292–13299, 2022. URL https://ieeexplore.ieee.org/abstract/document/9981157.

[7] J Jiao, P Yun, L Tai, and M Liu. Mlod: Awareness of extrinsic perturbation in multi-lidar 3d object detection for autonomous driving. In *Proceedings of the IEEE/RSJ International Conference on Intelligent Robots and Systems*, pages 10556–10563, 2020. URL https://ieeexplore.ieee.org/abstract/document/9341254.

[8] J. Jiao, H. Ye, Y. Zhu, and M. Liu. Robust odometry and mapping for multi-lidar systems with online extrinsic calibration. *IEEE Transactions on Robotics*, 38(1):351–371, 2021. URL https://ieeexplore.ieee.org/abstract/document/9444284.

[9] Y Jung, M Jeon, C Kim, S Seo, and S Kim. Uncertainty-aware fast curb detection using convolutional networks in point clouds. In *Proceedings of the IEEE International Conference on Robotics and Automation*, pages 12882–12888, 2021.

[10] Jiarong Lin, Xiyuan Liu, and Fu Zhang. A decentralized framework for simultaneous calibration, localization and mapping with multiple lidars. In *Proceedings of the IEEE/RSJ International Conference on Intelligent Robots and Systems*, pages 4870–4877, 2020. URL https://ieeexplore.ieee.org/document/9340790.

[11] J Lv, K Hu, J Xu, Y Liu, X Ma, and X Zuo. Clins: Continuous-time trajectory estimation for lidar-inertial system. In *Proceedings of the IEEE/RSJ International Conference on Intelligent Robots and Systems*, pages 6657–6663, 2021. URL https://ieeexplore.ieee.org/abstract/document/9636676.

[12] Gregory P Meyer and Niranjan Thakurdesai. Learning an uncertainty-aware object detector for autonomous driving. In *2020 IEEE/RSJ International Conference on Intelligent Robots and Systems (IROS)*, pages 10521–10527, 2020. URL https://ieeexplore.ieee.org/abstract/document/9341623.

[13] E Mueggler, G Gallego, H Rebecq, and D Scaramuzza. Continuous-time visual-inertial odometry for event cameras. *IEEE Transactions on Robotics*, 34(6):1425–1440, 2018. URL https://ieeexplore.ieee.org/abstract/document/8432102.

[14] T. Nguyen, S. Yuan, M. Cao, L. Yang, T. Nguyen, and L. Xie. Miliom: Tightly coupled multi-input lidar-inertia odometry and mapping. *IEEE Robotics and Automation Letters*, 6(3):5573–5580, 2021.

[15] Thien-Minh Nguyen, Shenghai Yuan, Muqing Cao, Yang Lyu, Thien H Nguyen, and Lihua Xie. Ntu viral: A visual-inertial-ranging-lidar dataset, from an aerial vehicle viewpoint. *International Journal of Robotics Research*, 41(3):270–280, 2022. URL https://journals.sagepub.com/doi/full/10.1177/02783649211052312.

[16] A. Reinke, M. Palieri, B. Morrell, Y. Chang, K. Ebadi, L. Carlone, and A. Agha-Mohammadi. Locus 2.0: Robust and computationally efficient lidar odometry for real-time 3d mapping. *IEEE Robotics and Automation Letters*, 7(4):9043–9050, 2022. URL https://ieeexplore.ieee.org/abstract/document/9793601.

[17] Y. Wang, W. Song, Y. Lou, F. Huang, Z. Tu, and S. Zhang. Simultaneous localization of rail vehicles and mapping of environment with multiple lidars. *IEEE Robotics and Automation Letters*, 7(3):8186–8193, 2022. URL https://ieeexplore.ieee.org/abstract/document/9810333.

[18] W Xu and F Zhang. Fast-lio: A fast, robust lidar-inertial odometry package by tightly-coupled iterated kalman filter. *IEEE Robotics and Automation Letters*, 6(2):3317–3324, 2021. URL https://ieeexplore.ieee.org/abstract/document/9372856.

[19] W. Xu, Y. Cai, D. He, J. Lin, and F. Zhang. Fast-lio2: Fast direct lidar-inertial odometry. *IEEE Transactions on Robotics*, 38(4):2053–2073, 2022. URL https://ieeexplore.ieee.org/abstract/document/9697912.